Cellulose (2022) 29:4153–4165
https://doi.org/10.1007/s10570-022-04555-0

ORIGINAL RESEARCH

Influence of delignification on plastic flow deformation of wood

Masako Seki · Yuko Yashima · Mitsuru Abe · Tsunehisa Miki · Masakazu Nishida

Received: 9 September 2021 / Accepted: 23 March 2022 / Published online: 2 April 2022

Abstract In this study, we elucidated the influence of delignification of wood on its plastic flow deformation caused by the shear sliding of wood cells. The delignified wood samples were characterized by attenuated total reflection-infrared (ATR-IR) spectroscopy, nuclear magnetic resonance (NMR) spectroscopy, Raman imaging analysis, and dynamic viscoelastic measurements. Then, the effects of the chemical structure, distribution, and molecular motility of lignin on the deformability of wood were evaluated. The delignified wood in water-swollen state was significantly deformed without cell wall destruction at a lower pressure than the untreated wood. The deformability was evaluated from two perspectives: stress at flow starting point and deformed cross-sectional area of the wood sample. The deformability of the delignified and untreated wood increased with increasing temperature during compression. In the early stages of delignification, the lignin in the compound middle lamella decreased, especially at the cell corner, which reduced the stress at the flow starting point. However, the deformed cross-sectional area of wood varied slightly with delignification time in these stages. As the delignification proceeded, the lignin at the vicinity of the polysaccharides in the cell wall was removed and the deformability improved significantly. Additionally, the stress at the flow starting point increased linearly with the peak temperature of tan δ, corresponding to the glass transition temperature of lignin in water-swollen wood, regardless of the temperature during compression. The correlation between chemical and physicochemical properties and plastic flow deformability presented in this paper will aid in low-energy and highly productive formation of solid-state wood.

Keywords Wood · Plastic deformation · Deformability · Delignification · NMR

Introduction

The deformation processing of wood can effectively promote its use in various applications, such as furniture, building, construction, automotive, and other daily necessities. Conventional methods of wood deformation include compression and bending processing using cell-wall deformations (Sandberg et al. 2012). These methods produce simple two-dimensional products, while retaining the cell arrangement and structure of the wood. On the other hand, reducing the element size of wood can

Supplementary Information The online version contains supplementary material available at https://doi.org/10.1007/s10570-022-04555-0.

M. Seki (✉) · Y. Yashima · M. Abe · T. Miki · M. Nishida
Multi-Materials Research Institute, National Institute of Advanced Industrial Science and Technology (AIST), 2266-98 Shimoshidami, Moriyamaku, Nagoya 463-8560, Japan
e-mail: m-seki@aist.go.jp

efficaciously enable the formation of more complex products. Wood-plastic composites (WPCs), which are a mixture of wood powder and plastic, are widely used as building materials (Spear et al. 2015). However, they require an input of energy to miniaturize the wood, which results in the destruction of the original cell structure, such that the products do not retain the wood texture. Furthermore, in conventional processing, the element size of wood and the complexity of the product shape have a contradictory relationship. To date, there have been few successful reports on the formation of a complex shape from solid-state wood.

Recently, a new technique, wood flow forming (WFF), has been developed, which can form complex shapes with solid-state wood because it takes advantage of plastic flow deformation (Abe et al. 2020, 2021; Miki et al. 2014a, 2014b, 2017; Seki et al. 2016; Yamashita et al. 2009). The wood is compressed in a heated mold, which enables it to flow plastically owing to the shear sliding between wood cells to produce a final shaped product (Miki et al. 2017). The application of traditional plastic forming techniques for metal and plastic materials yields efficiently wood products with simple processes. Although these techniques can critically affect the original cell arrangement of wood with high compressive stress, the original wood cell wall structure can be maintained to obtain a unique cell-derived texture of the product (Miki et al. 2014a). However, to improve the deformability of wood during the forming process and the durability of the products, it is necessary to modify the wood by pretreatment before forming. The cell wall and compound middle lamella (CML) are modified by impregnating the wood with resin monomers (Miki et al. 2014b; Seki et al. 2016) and/or chemical modification (Abe et al. 2020, 2021). WFF has great potential for various applications; however, it requires high temperatures (> 100 °C) and pressures (> 50 MPa), making it energy-intensive and less productive. To solve these problems, this study focused on lignin, which acts as an adhesive and binds the polysaccharides (cellulose and hemicellulose) and cells together. The lignin content is higher in CML than in cell walls (Kumar et al. 2021). Moreover, the wood cells are dissociated at the interface between the cells (i.e., CML) during the WFF process (Yamashita et al. 2009). Therefore, lignin, especially in CML, has a significant plastic flow effect.

Delignification is a process that can remove lignin without breaking the cellular structure of the wood, and it has primarily been studied for pulping wood. However, in recent years, delignified wood (DW) (Kumar et al. 2021) has attracted attention as a functional material for use in transparent wood (Li et al. 2016, 2017, 2020), high-strength structural materials (Frey et al. 2019b; Jakob et al. 2020; Song et al. 2018), high-performance thermal insulators (Li et al. 2018), and thermal energy storage materials (Montanari et al. 2019). Deformation processing that takes advantage of the flexibility of DW has also been developed (Khakalo et al. 2020; Frey et al. 2018, 2019a). Frey et al. (2019a) reported that a completely delignified veneer in a water-swollen state exhibited significant deformability in the fiber direction. As the improvement on deformability of DW has been reported, the plastic flow deformation associated with WFF is potentially affected by delignification.

The thermal softening properties of water-swollen wood depend on the glass transition of lignin (Kojiro et al. 2008; Nakajima et al. 2009). When the molecular mass of lignin in wood decreases, its glass transition temperature also decreases, in turn significantly softening the wood (Nakajima et al. 2009). Therefore, it is expected that the changes in lignin due to delignification will promote the plastic flow deformation of wood and reduce the production energy required for WFF.

The objective of this study was to elucidate the effect of delignification on the plastic flow deformation of wood. DW and untreated-wood (UW) samples with different molecular masses and amounts of lignin were prepared by subjecting them to delignification and varying the delignification time. Free compression testing was used to evaluate the deformability of the samples based on the stress at the flow starting point and the deformed cross-sectional area of the wood sample. The samples were characterized by attenuated total reflection-infrared (ATR-IR) spectroscopy, nuclear magnetic resonance (NMR) spectroscopy, Raman imaging analysis, and dynamic viscoelastic measurements. The effects of the amount, chemical structure, distribution, and molecular motilities of lignin on the plastic flow deformation of wood are discussed as well.

Materials and methods

Materials

Wood samples were successively cut in the longitudinal (L) direction from a block of sapwood of a Japanese cypress (*Chamaecyparis obtusa*) log collected from the Kiso region of Japan. The dimensions of the samples used for the dynamic viscoelastic measurements were 1 mm (L)×30 mm (radial (R) direction)×3 mm (tangential (T) direction). The samples for the other measurements (ATR-IR, NMR, Raman imaging analysis, and free compression testing) had dimensions of 5 mm (L)×5 mm (R)×5 mm (T). Prior to delignification, the wood samples were pre-treated with approximately 100 °C distilled water for 4 h, followed by methanol for 6 h to remove the low-molecular-weight components. The pre-treated samples were then dried at 50 °C for 18 h and 105 °C for 2 h to a relatively constant mass (m_0). One side of the RT surface of some samples (5 mm×5 mm×5 mm) was microtome-finished prior to subsequent delignification.

Preparation of delignified wood samples

The pre-treated samples were delignified using an acetic acid solution containing 4 wt% sodium chlorite ($NaClO_2$) (pH 3). The $NaClO_2$ solution was impregnated into the pre-treated samples under vacuum, and the impregnated samples were treated at 45 °C for several reaction times (t_r) of 10, 30, 60, 180, or 360 min. Then, the DW samples were washed several times with distilled water and stored in water at 20–25 °C Note that the DW sample with a t_r longer than 360 min was brittle and fragile; therefore, it was considered unsuitable for WFF and was not evaluated in this study. In addition, the UW samples were impregnated with distilled water, instead of the $NaClO_2$ solution, at 20–25 °C for 500 min or more (t_r: 0 min).

The area in the RT cross section of the water-swollen DW and UW samples (s_d and s_u, respectively) was measured, and the area increase rate (A_{RT}) of the water-swollen samples due to delignification was calculated using the following formula:

$$A_{RT} = \left(s_d - s_u\right)/s_u \times 100\,[\%] \tag{1}$$

Some of the water-swollen samples were then dried at 35 °C for 24 h, at 50 °C for 18 h, and at 105 °C for 3 h to a relatively constant mass (m_t). The mass loss (*ML*) due to delignification of the dried samples was calculated using the following formula:

$$ML = \left(m_o - m_t\right)/m_o \times 100\,[\%] \tag{2}$$

Acetyl bromide method for quantification of lignin

The acetyl bromide method for quantifying lignin derived from wood is advantageous, because it is rapid, simple, and appropriate for small sample sizes (Hatfield and Fukushima 2005). The milled dried samples (5 mg) were placed in a glass reaction vial with 5 mL of 25% (v/v) acetyl bromide in acetic acid and 0.2 mL of perchloric acid (60%); the vial was subsequently sealed and heated at 70 °C for 30 min. After cooling, the contents of the vial were quantitatively transferred to a 100-mL volumetric flask containing 10 mL of 2 M NaOH and 25 mL of acetic acid, and the volume was made up to 100 mL with acetic acid. The UV absorption spectrum was measured with a UV–vis spectrophotometer (UV-3600; Shimadzu Corporation, Kyoto, Japan) at 280 nm. Ultimately, the lignin content (*LC*) was calculated using the following equation:

$$LC = A_s \times V/(k \times W) \times 100[\%] \tag{3}$$

where A_s represents the absorbance of sample, k represents an absorption coefficient of standard lignin (=20.09), V represents the volume of solution, and W denotes the weight of the sample.

Attenuated total reflection infrared (ATR-IR) spectroscopy.

The block-shaped sample (5 mm×5 mm×5 mm) in the dry state was cut in half in the L-direction, and ATR-IR measurements were performed near the center of the cut surface (RT surface, that is, near the center of the wood sample). The ATR-IR spectra were measured on a Nicolet 6700 spectrometer (Thermo Scientific Inc., Waltham, MA, USA) at a resolution of 4 cm^{-1} in the standard ATR mode; 32 scans were performed in the wavenumber range of 4000–700 cm^{-1}.

Nuclear magnetic resonance (NMR) spectroscopy

Solid-state ^{13}C NMR spectra were measured on a Varian 400 NMR system spectrometer (Palo Alto, CA) with a Varian 4 mm double-resonance T3 solid

probe. A thin sample (approximately 0.1 mm) was cut out from near the surface, shredded, and then used for NMR measurement. The shredded samples were placed in a 4 mm ZrO_2 rotor spun at 15 kHz within a temperature range of 20–22 °C. The ^{13}C cross-polarization and magic-angle spinning (CP-MAS) NMR spectra were collected with a 2.6-μs π/2 pulse at 100.56 MHz for the ^{13}C nuclei and an acquisition period of 40 ms over a spectral width of 30.7 kHz. Proton decoupling was performed with an 86 kHz ^{1}H decoupling radio frequency with a small phase incremental alteration (SPINAL) decoupling pulse sequence. The ^{1}H-^{13}C cross-polarization for the spectrum acquisition was conducted with a 5.0 s recycle delay in 1024 transients using a ramped-amplitude pulse sequence with a contact time of 2 ms and a 2.6-μs π/2 pulse for the ^{1}H nuclei. The amplitude of the ^{1}H nuclei was linearly ramped down from 92.6% of its final value during the CP contact time. The ^{1}H spin–lattice relaxation time in the laboratory frame (T_1H) was indirectly measured by detecting the ^{13}C resonance enhanced by the cross-polarization in the ^{13}C CP-MAS sequence, and was applied after a π pulse to ^{1}H nuclei using the inversion recovery method. The T_1H analysis of the sample was carried out using the same solid-state probe used to obtain the ^{13}C CP-MAS NMR spectra of the sample at the same contact time and acquisition period.

Raman imaging analysis

The block-shaped sample (5 mm × 5 mm × 5 mm) in the water-swollen state were sectioned to 25-μm-thick cross-sections with a rotary microtome (RMS; Nihon Microtome Laboratory, Inc., Osaka, Japan). These thin sections were placed between glass slides and coverslips with a drop of water. Thereafter, these sections were analyzed using a confocal micro-Raman system (LabRAM HR-800MX; Horiba, Ltd., Kyoto, Japan) equipped with a confocal microscope (BX41, Olympus, Tokyo, Japan), a 50 × air objective (LMPLFLN; NA = 0.5, Olympus, Tokyo, Japan), and a 514 nm argon ion laser (Series 532; Melles Griot Laser Group, Carlsbad, CA, USA). In particular, the incident laser power was 20 mW, and the Raman signal was detected by an air-cooled charge-coupled device (CCD) camera situated behind a 600 lines/mm grating. The mapping was recorded with an integration period of 0.3 s and a step size of 300 nm. Moreover, the LabSpec5 software (Horiba, Ltd.) was used for image processing, and the raw spectral data were baseline corrected to remove the background from the fluorescence.

Dynamic viscoelastic measurement

The temperature dependence of the loss tangent (tan δ) was measured by the tensile forced oscillation method using a thermomechanical analysis apparatus (TMA SS6100; Hitachi High-Tech Science Corp., Tokyo, Japan). The water-swollen sample (1 mm (L) × 30 mm (R) × 3 mm (T)) immersed in water was subjected to a temperature increase from 30 to 100 °C at a rate of 0.5 °C/min. The frequencies for the measurement were 0.01 Hz; the span was 18 mm in the R-direction; and the load amplitude was 70 ± 20 mN. Viscoelastic behavior is sensitive to the drying and heat history of the samples before the measurement (Kojiro et al. 2008). To unify the histories of the samples, they were heated to 100 °C, naturally cooled down to approximately 20 °C, and then subjected to measurements in the water-swollen state.

Free compression testing

A uniaxial compression test was carried out using a material testing machine (CATY TC-2kN-NS; Yonekura Mfg. Co. Ltd., Osaka, Japan) (Fig. 1). The testing machine equipped with a container enables horizontal compression tests of samples in a water-swollen state under confined heating conditions while recording load-stroke curves during hydrothermal compression. The temperature during compression (T_c) was controlled by heating the water with a cartridge heater immersed in a water pit.

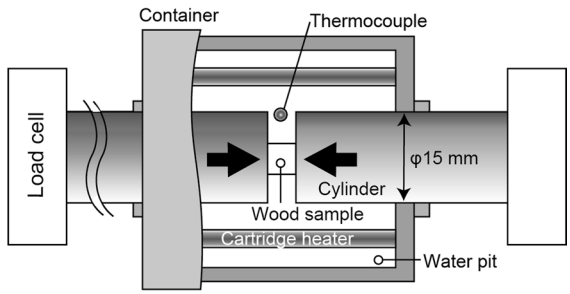

Fig. 1 Schematic of the experimental apparatus

The container was sealed and heated until the temperature detected by the thermocouple stabilized to the target temperature (T_c). Then, the water-swollen sample was placed between the cylinders (diameter: 15 mm) under 2–3 N to ensure that the R was in the compression direction. The container was closed again to heat the sample to a constant temperature under saturated steam. Five minutes after achieving the temperature T_c, compression testing was conducted at a constant speed of 1 mm/min up to 3000 N of the compression load or until the maximum stroke of 5 mm of the testing machine. T_c was set to 40, 60, 80, and 100 °C in consideration of the decrease in the glass transition temperature of lignin due to delignification (Nakajima et al. 2009). Compression testing was conducted using three or more samples under the same conditions.

For one sample under each condition, the container was opened after compression testing, and the compressed sample was dried at room temperature to retain its shape while maintaining the stroke after testing, followed by further drying at 105 °C for 1 h. Then, the mass (m_d) and thickness (r_c) in the compression direction were measured. The final compression ratio (C_d) was calculated as follows:

$$C_d = \left(r_b - r_c\right)/r_b \times 100[\%] \quad (4)$$

where r_b is the dimension in the R-direction of the water-swollen sample before the compression testing. The appearance of the compressed sample from the LT planes was observed using an optical microscope (VHX-970F; Keyence Corp., Osaka, Japan). The deformed cross-sectional area of the LT planes before and after compression testing was calculated by binarizing the captured image, and the area magnification (AM_d) was calculated as follows:

$$AM_d = A_c/A_b \times 100[\%] \quad (5)$$

where A_b and A_c are the areas of the deformed cross-sectional area of the water-swollen sample before compression and the dried sample after compression, respectively.

Results and discussion

Characterization of untreated and delignified samples

The mass loss and the area increase rate

Figure 2 shows the variation in *mass loss* (*ML*) (left axis, closed circles) and area increase rate (A_{RT}) (right axis, open circles) as functions of delignification time (t_r). *ML* linearly increased with increasing delignification time. The A_{RT} also increased with increasing delignification time, indicating that delignification increased the wood dimensions in a water-swollen state. The increase in the dimensions of the water-swollen sample was caused by the swelling of the cell wall and CML. The total volume of the adsorbed water in the cell wall and CML exceeded the volume of lignin removed by delignification, which implied that the lignin removal increased the porosity and facilitated the water uptake.

Lignin content

The variation in lignin content (*LC*) obtained from the acetyl bromide method as a function of delignification time (t_r) is plotted in Fig. 3, which depicts the logarithmic decreases in *LC* with increasing t_r. The *LC* of UW samples ($t_r = 0$ min) was approximately 32%, which is consistent with previous reports (Pettersen 1984). After the longest t_r ($t_r = 360$ min), the *LC* decreased by approximately 13% from that of UW. The final value of *ML* expressed in Fig. 2 was very similar (13% of *ML* at $t_r = 360$ min). Therefore, the contents of wood constituents other than lignin,

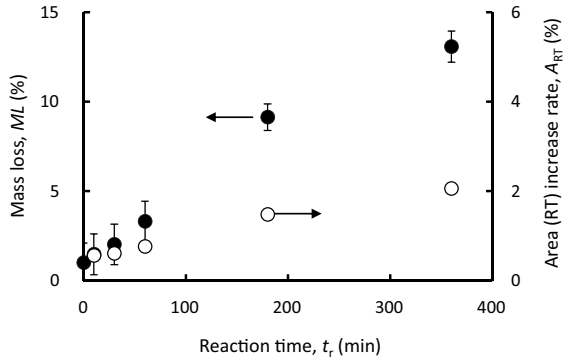

Fig. 2 Variation of mass loss (*ML*) and area increase rate (A_{RT}) with delignification time (t_r)

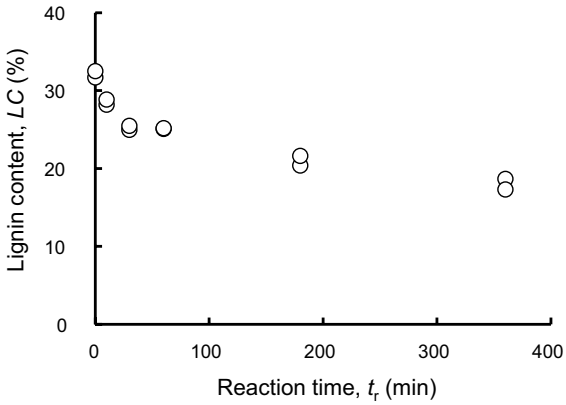

Fig. 3 Variation of lignin content (*LC*) with delignification time (t_r)

such as polysaccharides, did not reduce after the delignification.

ATR-IR spectroscopy

Figure 4 shows the ATR-IR spectra of the UW and DW samples, which indicate that the chemical structure of the wood sample changes with delignification. The area of the peak at 1490–1530 cm^{-1}, which corresponds to the skeletal vibrations of the benzene ring in lignin, decreased with increasing delignification time. This indicates the initiation of the reaction during the early stages of delignification, as the benzene rings of lignin start to disappear. This tendency is consistent with that of the *LC* (Fig. 3) calculated from the UV absorbance of the benzene rings. The absorbance peak at 1725–1750 cm^{-1} corresponding to the C=O stretch of lignin and hemicellulose initially increased (t_r = 10 min) before decreasing in the later stages (t_r = 360 min). The initial increase in this peak can be attributed to the reaction between $NaClO_2$ and lignin, which indicates that the aromatic ring was cleaved (Li et al. 2017). On the other hand, the decrease in the later stage was due to the decrease in the amount of lignin. The initial structural changes of lignin due to delignification consisted of the elimination and cleavage of the benzene ring, followed by the elimination of the benzene ring.

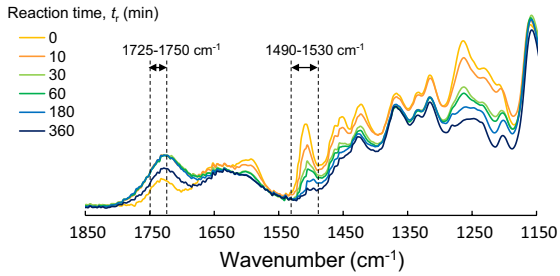

Fig. 4 ATR-IR spectra of the untreated-wood (UW, t_r = 0 min) and delignified wood (DW, t_r = 10, 30, 60, 180 and 360 min) samples in the dry state

Solid state NMR measurements

Figure 5 shows the ^{13}C cross-polarization (CP) MAS NMR spectra for each substituent in the UW and DW samples. Signals corresponding to biomass constituents in the wood were assigned based on our previous report (Nishida et al. 2014). The carbohydrates appeared as relatively large and sharp signals in the range of 60–110 ppm. However, most of the signals for cellulose and hemicellulose, except cellulose C4, overlapped with each other, and the crystalline and amorphous

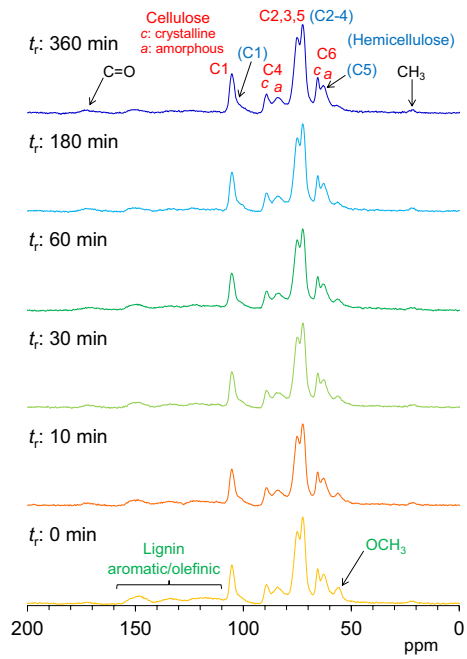

Fig. 5 ^{13}C CP-MAS NMR spectra of untreated wood (UW, t_r = 0 min) and delignified wood (DW, t_r = 10, 30, 60, 180 and 360 min) samples in dry state

signals for cellulose C4 and C6 could be separately observed. The aromatic and olefinic groups in lignin appeared as broader signals in the range of 110–160 ppm, while the methoxy groups in lignin appeared as isolated signals at 56 ppm.

During the early stages of delignification ($t_r = 10$ min), the signal intensity of the OCH_3 (56 ppm) and aromatic (110–160 ppm) groups in lignin rapidly decreased was observed. Meanwhile, the intensity of the C = O signal at a lower magnetic field (172 ppm) increased for 30 min, then gradually decreased as delignification progressed. The trends of the signal intensities for the aromatic and C = O groups in the ^{13}C CP-MAS NMR spectra were similar to those in the ATR-IR spectra (Fig. 4). Therefore, in the first step of delignification, oxidation of the benzene ring of the guaiacyl unit on the surface of the lignin unit afforded two carboxyl groups at C3 and C4 positions (Hamzeh et al. 2008). Next, the cleavage of C–C and C–O bonds that provide bridging with other aromatic ring units at the inner site of the lignin resulted in higher *ML* of the delignified wood, because the oxidized portion was removed (Tarvo et al. 2010 and Qu et al. 2020). However, the signal pattern of the carbohydrates in the ^{13}C CP-MAS NMR spectra barely changed as a result of delignification, indicating that the chemical structures of cellulose and hemicellulose remained unchanged as delignification progressed.

Figure 6 shows the ^{1}H spin–lattice relaxation times in the laboratory frame (T_1H) of the dry samples. A minimal change was observed in the T_1H values at 65 and 75 ppm for $t_r = 60$ min, but tended to increase after 60 min. For wood in the dry state, the spin–lattice relaxation for each wood constituent occurs via lignin, which has the shortest T_1H value among the biomass constituents (Nishida et al. 2017). The increase in T_1H of the DW samples at $t_r > 60$ min was caused by the loss of lignin units with the short T_1H values. In the early stages ($t_r \leq 60$ min), delignification occurred at the distal part of the polysaccharide chain, with minimal effect on the polysaccharides. With increasing t_r (> 60 min), the reaction progressed toward the polysaccharide chain, resulting in an increase in the because of the reduced interactions between the polysaccharides and lignin.

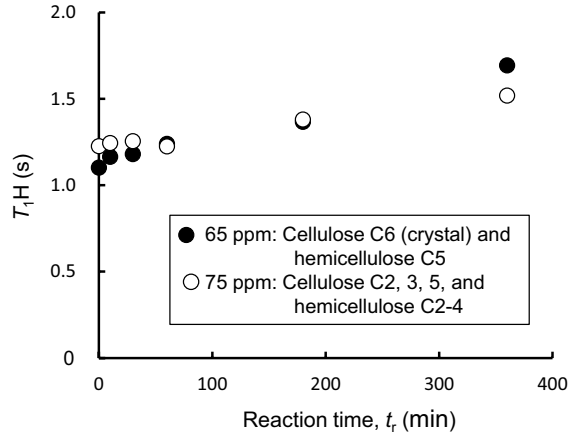

Fig. 6 ^{1}H spin–lattice relaxation time in the laboratory frame (T_1H) of the untreated wood (UW, $t_r = 0$ min) and delignified wood (DW, $t_r = 10$, 30, 60, 180 and 360 min) samples in the dry state at 65 and 75 ppm

Raman imaging analysis

The variations in the cellular-scale distribution of lignin with delignification were visualized by the Raman imaging technique (Fig. 7 (g–l)). Raman images were obtained by integration of the absorption bands between 1525 cm^{-1} and 1700 cm^{-1} (Fig. S1), assigned to the aromatic lignin vibrations (Segmehl et al. 2019). In the untreated sample (g), the lignin content was higher in CML than cell wall and the highest at the cell corners. The lignin distribution varied specifically in the early stages of delignification ($t_r \leq 60$ min), in which the lignin in CML located particularly at the cell corner decreased with delignification (g–j). With increasing t_r (> 60 min), both lignin in CML and cell wall gradually reduced (j–l). Therefore, the delignification initiated at the distal part of the polysaccharide chain in the early stages (Fig. 6, $t_r \leq 60$ min) progressed from the CML rather than from the cell wall. Thereafter ($t_r > 60$ min), the decrease in cell wall lignin (Fig. 7(j–l)) reduced the lignin interaction with polysaccharides that are abundant in the cell wall, as indicated by the results of T_1H (Fig. 6).

Dynamic viscoelastic measurement

Figure 8 shows the temperature dependence of tan δ for the water-swollen samples. The tan δ peak is attributable to the glass transition of lignin, and the

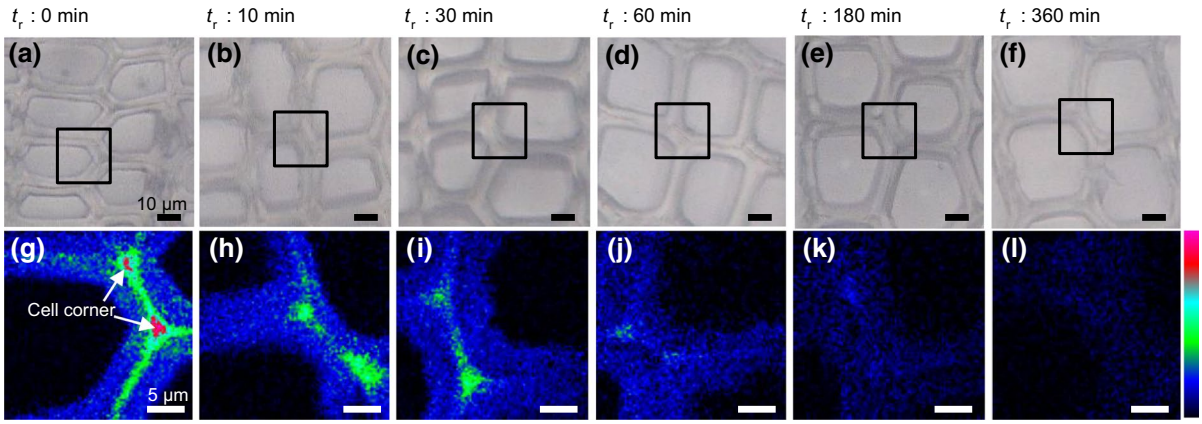

Fig. 7 Optical microscopy images (a–f) and Raman images based on intensity of spectral region assigned to aromatic lignin (1525–1700 cm^{-1}, g–l) on the cross-section of the untreated wood (UW, $t_r = 0$ min) and delignified wood (DW, $t_r = 10$, 30, 60, 180 and 360 min) sample in water-swollen state. Squares in optical microscopy images (a–f) denote measured positions of Raman images (g–l)

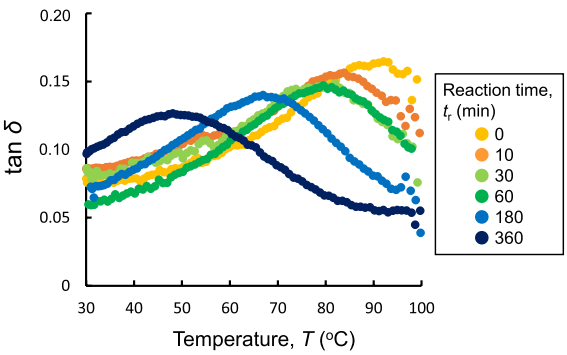

Fig. 8 Temperature dependence of tan δ of untreated wood (UW, $t_r = 0$ min) and delignified wood (DW, $t_r = 10$, 30, 60, 180 and 360 min) samples in the water-swollen state

peak temperature (*T*g) in Fig. 8 corresponds to the glass transition temperature of lignin in the wood samples (Kojiro et al. 2008; Nakajima et al. 2009). As delignification progressed, the *T*g shifted to the lower temperature and the shape of the peak broadened because of the varying molecular weight distribution. These trends correspond well with those by Nakajima et al. (2009). In general, the shift of *T*g to a lower temperature indicates the reduction of molecular motility constraints, such as the decrease in molecular weight. In case of the wood in water-swollen state, the shift of *T*g was caused by the reduction in the lignin molecular weight as well as the increased porosity and adsorbed water in the lignin molecules by delignification (Fig. 2). The results in Fig. 8 reveal that these modifications initiated during the early stages of delignification ($t_r = 10$ min).

Deformability of untreated and delignified samples

Figure 9 shows the relationship between the nominal compressive stress (σ) and the compression ratio (C) during compression testing at each T_c. The σ slightly increased to a C of approximately 60% in all samples, during which the cell lumens in the wood samples gradually closed because of the buckling of the cell wall. As C increases, σ significantly increase, followed by an inflection point at which the rate of increase in σ decreases (indicated by the arrow in Fig. 9). These compressive behaviors were similar to those observed in our previous report (Miki et al. 2017). Before the inflection point, the cell lumens were completely closed and the sample was consolidated, resulting in a rapid increase in σ. After the inflection point, the rate of increase in σ decreased because the wood sample plastically deformed in the unconstrained direction (L or T). The inflection point was also detected in the flat region for $t_r = 360$ min at 100 °C (shown by (d) ▽); under this condition, plastic deformation occurred before the cell lumens were completely closed. The inflection points were not detected at 40 °C, 60 °C, and 80 °C for $t_r = 360$ min and at 100 °C for $t_r = 180$ min. This is because the inflection points due to the plastic

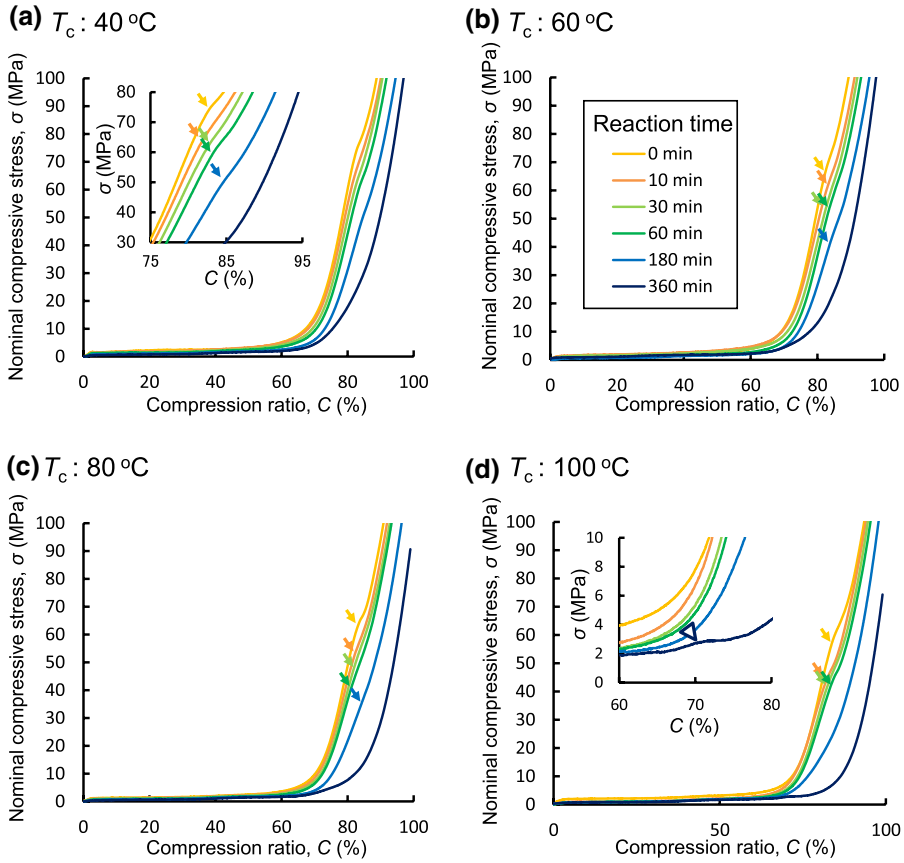

Fig. 9 Relationship between the nominal compressive stress (σ) and compression ratio (C) during compression testing at each temperature during compression (T_c)

deformation overlapped with the region denoting the rapid increase in σ.

The σ at the inflection point detected in Fig. 9 is the nominal compressive stress at the flow starting point (σ_y), which indicates the initial resistance of the samples to plastic flow. Regardless of temperature, the longer the delignification time, the smaller the σ_y. Therefore, the delignification process reduced the initial resistance to plastic flow.

Figure 10 shows photographs of the samples that were dried after free compression testing to preserve their shape. After compression testing, all the samples were able to maintain their deformed state after drying by pressure; they only deformed on T-direction, and not in the L-direction. Such anisotropy of

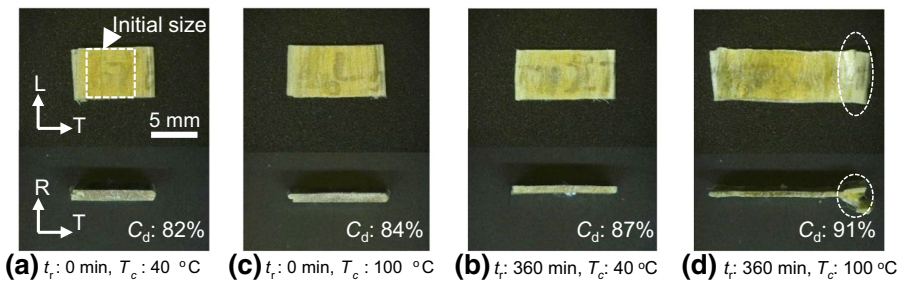

Fig. 10 Photographs of the untreated wood (UW, t_r=0 min) and delignified wood (DW, t_r=360 min) samples whose shape was fixed by drying post-free compression testing. The final compression ratio (C_d) is shown in each photograph. The part surrounded by the dotted line of the circle shows the sample protruding from the cylinders of the testing machine

plastic flow deformation is consistent with the phenomenon observed in our previous report (Miki et al. 2017). At high T_c, the sample that was delignification for a longer time exhibited the highest C_d of 91% (Fig. 10d), indicating that a considerably thin product could be fabricated from solid-state wood.

Figure 11 shows an SEM image of the RT surface of the samples. None of the samples displayed cell wall destruction. Furthermore, evidence of mutual positional change between the cells was confirmed. The plastic flow deformation was mainly caused by the shear sliding phenomenon between the cells and at the boundary of the CML. The sample subjected to a longer delignification time (Fig. 11c, d) displayed several slip surfaces, and plastic flow occurred in units with a smaller number of cells. The UW samples (Fig. 11a, b) appeared to be significantly compressed prior to flow deformation, whereas the DW samples (Fig. 11c, d) exhibited lesser compression than UW. In addition, the delignification impacted the strength of linkages in the R- and T-direction; therefore, the samples exposed to longer delignification could slip in R- and T- direction without undergoing significant densification process, as depicted in Fig. 11. The cells slightly protruding in the L-direction were also observed, suggesting that delignification promoted slip deformation in the L-direction.

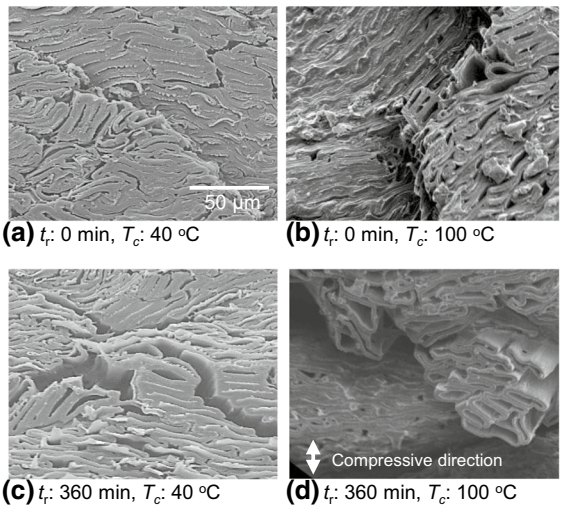

Fig. 11 The SEM images of the radial-tangential surfaces of untreated wood (UW, $t_r = 0$ min) and delignified wood (DW, $t_r = 360$ min) samples after free compression testing

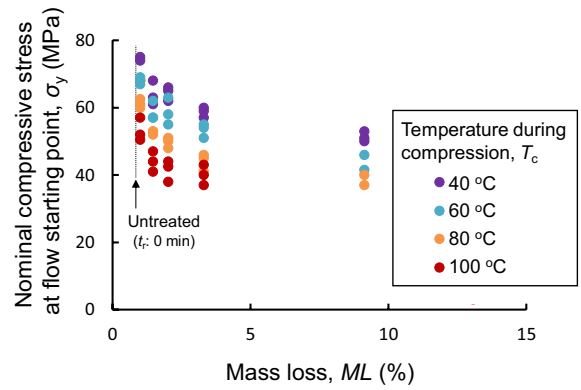

Fig. 12 Relationship between the mass loss (*ML*) by delignification of wood samples and nominal compressive stress at flow starting point (σ_y). The results of reaction time (t_r) of 180 min at 100 °C and t_r of 360 min were not described because the inflection point could not be detected after the consolidation of the sample in Fig. 9

Influence of delignification on plastic flow deformation of wood

The relationship between the *ML* by the delignification of wood samples and σ_y is illustrated in Fig. 12, which portrays the initial resistance of the wood samples toward plastic flow. More specifically, a higher T_c corresponds to a lower σ_y that was logarithmically reduced to a *ML* of 4%, thereby indicating a significant improvement of the plastic deformability in the early stages of delignification. Furthermore, the decrease in lignin from CML during the early stage of delignification (Fig. 7g–j) potentially reduced the linkage strength between cells, and consequently, decreased the initial resistance of the wood samples toward plastic flow.

The deformability was evaluated using the AM_d calculated from the deformed cross-sectional area of wood samples. Figure 13a shows the relationship between *ML* and the AM_d of the wood samples. The AM_d increased with increasing T_c. The value of AM_d was almost unchanged during the early stages of delignification ($ML \leq 4\%$); however, as delignification progressed, AM_d remarkably increased. The value of AM_d reached a maximum of 2.7 times for the longest t_r of 360 min at the highest T_c of 100 °C. Furthermore, delignification caused a change in the density of the sample; therefore, the area per unit mass (A_d/m_d), which is an index of deformability, was calculated based on the area of the LT surface (A_d)

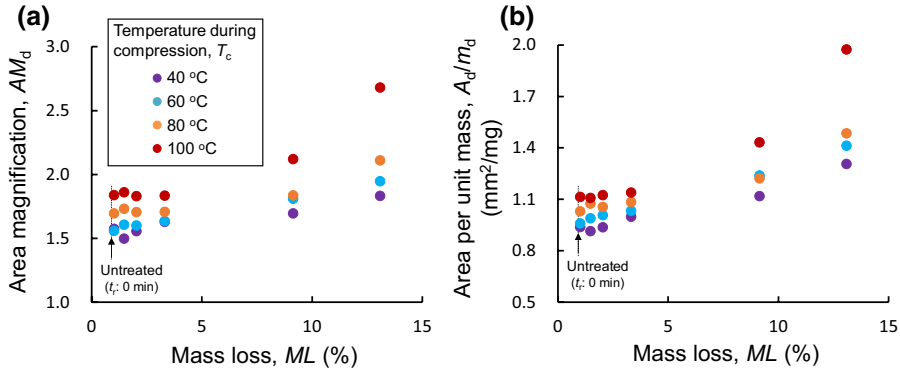

Fig. 13 Relationship between mass loss (*ML*) by delignification and area magnification (AM_d, a), and area per unit mass (A_d/m_d, b) of the wood samples

and the mass (m_d) of the dried compressed samples. The relationship between *ML* and A_d/m_d of the wood samples is shown in Fig. 13b. The change in A_d/m_d depending on the T_c and the tendency toward *ML* were similar to those of AM_d (Fig. 13a). In contrast to the tendency of σ_y in Fig. 12, the deformability evaluated from the deformed cross-sectional area did not increase during the early stages of delignification ($ML \leq 4\%$), but a significant increase was observed after a *ML* of 4% ($t_r > 60$ min). Delignification with $NaClO_2$ initially proceeds from the lignin-rich CML during the early stages of the reaction (Fig. 7g–j) and selectively softens the CML region. Then, the reaction and softening of the cell wall progresses during the later stages of the reaction (Fig. 7 (k, l), Xu et al. 2020). The results of T_1H (Fig. 6) suggest that the lignin removal in the vicinity of the polysaccharide chains that make up the cell wall proceeds during the later stages of delignification ($t_r > 60$ min), which can increase the flexibility of the cell wall. Those cell wall flexibility contributed to the increased deformability.

A strong correlation is observed between the *Tg* (Fig. 8) and σ_y (Fig. 12), as shown in Fig. 14. Regardless of *Tc*, the σ_y linearly increased with *Tg* following the same slope. This indicates the enhancement of lignin molecular motility, which was influenced by the reduction in the lignin molecular mass and the increased amount of adsorbed water among the lignin molecules, significantly contributed toward the improved deformability at the initial state of plastic flow. Because the plastic flow of wood was shear failure originating from the CML (Fig. 11), structural defects in the CML generated during the early stages of delignification, such as decrease in lignin at the cell corners (Fig. 7), considerably affect the initiation of plastic flow.

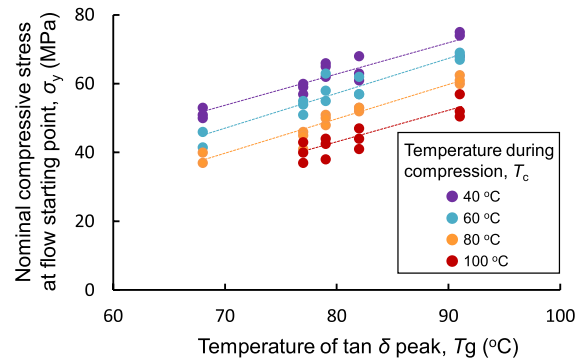

Fig. 14 The relationship between the peak temperature of tan δ (*Tg*) from Fig. 8 and the σ_y from Fig. 12. *Tg* is the average of three measurements

Conclusion

We clarified the influence of delignification on plastic flow deformation due to the shear sliding between wood cells. The deformability was evaluated by the stress at the flow starting point and deformed cross-sectional area of wood samples obtained by free compression testing. The lignin content in the wood gradually decreased with delignification time. The ATR-IR and solid-state NMR spectroscopic analyses of delignification showed that the oxidative opening of guaiacyl ring on the surface of the lignin unit occurred in the early stages and the oxidized portion was released from the inner site of the lignin unit when delignification time was extended. Raman imaging analysis revealed that the lignin in CML decreased significantly, especially at the cell corner, followed by both lignin in CML and cell wall were reduced. In the early stages of delignification, the decrease in lignin in the CML reduced the stress at

flow starting point. However, the deformed cross-sectional area of wood exhibited slight variations with delignification time during delignification in the early stages. In the later stages of delignification, the reaction possibly reached up to the vicinity of polysaccharide chains, causing larger deformations in the samples. Moreover, the stress at the flow starting point linearly increased with the peak temperature of tan δ corresponding to the glass transition temperature of lignin in water-swollen wood, regardless of the temperature during compression. The strategy of controlling the molecular mass and amount of lignin via delignification can yield more productive materials, as well as metal and plastic materials for achieving low-energy plastic flow deformation of wood. In this study, we examined delignified wood in the water-swollen state, but in the future, we plan to investigate the effect of other adsorbents, such as resin monomers, instead of water, on the plastic deformability of delignified wood.

Acknowledgments The authors like to thank the Asahi Kasei Corporation for financial support towards this study.

Funding This study was financially supported by Asahi Kasei Corporation.

Availability of data and material The data that support the findings of this study are available from the corresponding author, Masako Seki, upon reasonable request.

Code availability Not applicable.

Declarations

Conflicts of interest The authors declare no conflict of interest.

Ethics approval Not applicable.

Human and animal rights Additional declarations for articles in life science journals that report the results of studies involving humans and/or animals.

Not applicable.

Consent to participate We agreed.

Consent for publication We agreed.

References

Abe M, Enomoto Y, Seki M, Miki T (2020) Esterification of solid wood for plastic forming. BioResources 15(3):6282–6298. https://doi.org/10.15376/biores.15.3.6282-6298

Abe M, Seki M, Miki T, Nishida M (2021) Effect of the propionylation method on the deformability under thermal pressure of block-shaped wood. Molecules 26(12):3539. https://doi.org/10.3390/molecules26123539

Frey M, Widner D, Segmehl JS, Casdorff K, Keplinger T, Burgert I (2018) Delignified and densified cellulose bulk materials with excellent tensile properties for sustainable engineering. ACS Appl Mater Interfaces 10(5):5030–5037. https://doi.org/10.1021/acsami.7b18646

Frey M, Biffi G, Adobes-Vidal M, Zirkelbach M, Wang Y, Tu K, Hirt AM, Masania K, Burgert I, Keplinger T (2019a) Tunable wood by reversible Interlocking and bioinspired mechanical gradients: moisture triggered reversible interlocking between neighboring cells. Adv Sci 6(10):1802190. https://doi.org/10.1002/advs.201802190

Frey M, Schneider L, Masania K, Keplinger T, Burgert I (2019b) Delignified wood−polymer interpenetrating composites exceeding the rule of mixtures. ACS Appl Mater Interfaces 11(38):35305–35311. https://doi.org/10.1021/acsami.9b11105

Hamzeh Y, Mortha G, Lachenal D, Izadyar S (2008) Selective degradation of lignin polymer by chlorine dioxide during chemical pulp delignification in flow through reactor. Polymer Plast Tech Eng 47:931–935. https://doi.org/10.1080/03602550802274506

Hatfield R, Fukushima RS (2005) Can lignin be accurately measured? Crop Sci 45(3):832–839. https://doi.org/10.2135/cropsci2004.0238

Jakob M, Stemmer G, Czabany I, Müller U, Gindl-Altmutter W (2020) Preparation of high strength plywood from partially delignified densified wood. Polymers 12(8):1796. https://doi.org/10.3390/polym12081796

Khakalo A, Tanaka A, Korpela A, Orelma H (2020) Delignification and ionic liquid treatment of wood toward multifunctional high-performance structural materials. ACS Appl Mater Interfaces 12(20):23532–23542. https://doi.org/10.1021/acsami.0c02221

Kojiro K, Furuta Y, Ishimaru Y (2008) Influence of histories on dynamic viscoelastic properties and dimensions of water-swollen wood. J Wood Sci 54:95–99. https://doi.org/10.1007/s10086-007-0926-4

Kumar A, Jyske T, Petrič M (2021) Delignified wood from understanding the hierarchically aligned cellulosic structures to creating novel functional materials: a review. Adv Sustain Syst 5(5):2000251. https://doi.org/10.1002/adsu.202000251

Li Y, Fu Q, Yu S, Yan M, Berglund L (2016) Optically transparent wood from a nanoporous cellulosic template: combining functional and structural performance. Biomacromol 17(4):1358–1364. https://doi.org/10.1021/acs.biomac.6b00145

Li Y, Fu Q, Rojas R, Yan M, Lawoko M, Berglund L (2017) Lignin-retaining transparent wood. Chemsuschem 10(17):3445–3451. https://doi.org/10.1002/cssc.201701089

Li T, Song J, Zhao X, Yang Z, Pastel G, Xu S, Jia C, Dai J, Chen C, Gong A, Jiang F, Yao Y, Fan T, Yang B, Wågberg L, Yang R, Hu L (2018) Anisotropic, lightweight, strong, and super thermally insulating nanowood with naturally

aligned nanocellulose. Sci Adv 4(3):3724. https://doi.org/10.1126/sciadv.aar3724

Li K, Wang S, Chen H, Yang X, Berglund L, Zhou Q (2020) Self-densification of highly mesoporous wood structure into a strong and transparent film. Adv Mater 32(42):2003653. https://doi.org/10.1002/adma.202003653

Miki T, Seki M, Tanaka S, Shigematsu I, Kanayama K (2014a) Preparation of three dimensional products using flow deformability of wood treated by small molecular resins. Adv Mater Res 856:79–86. https://doi.org/10.4028/www.scientific.net/AMR.856.79

Miki T, Sugimoto H, Shigematsu I, Kanayama K (2014b) Superplastic deformation of solid wood by slipping cells at submicrometer intercellular layers. Int J Nanotechnol 11(5/6/7/8):509–519. https://doi.org/10.1504/IJNT.2014.060572

Miki T, Nakaya R, Seki M, Tanaka S, Sobue N, Shigematsu I, Kanayama K (2017) Large deformability derived from a cell–cell slip mechanism in intercellular regions of solid wood. Acta Mech 228(8):2751–2758. https://doi.org/10.1007/s00707-015-1523-z

Montanari C, Li Y, Chen H, Yan M, Berglund L (2019) Transparent wood for thermal energy storage and reversible optical transmittance. ACS Appl Mater Interfaces 11(22):20465–20472. https://doi.org/10.1021/acsami.9b05525

Nakajima M, Furuta Y, Ishimaru Y, Ohkoshi M (2009) The effect of lignin on the bending properties and fixation by cooling of wood. J Wood Sci 55:258–263. https://doi.org/10.1007/s10086-009-1019-3

Nishida M, Tanaka T, Miki T, Shigematsu I, Kanayama K, Kanematsu W (2014) Study of nanoscale structural changes in isolated bamboo constituents using multiscale instrumental analyses. J Appl Polym Sci 131:40243. https://doi.org/10.1002/app.40243

Nishida M, Tanaka T, Miki T, Hayakawa Y, Kanayama K (2017) Instrumental analyses of nanostructures and interactions with water molecules of biomass constituents of Japanese cypress. Cellulose 24:5295–5312. https://doi.org/10.1007/s10570-017-1507-3

Pettersen RC (1984) The chemical composition of wood. In: Rowell RM (ed) The Chemistry of Solid Wood, Advances in Chemistry Series, vol 207. American Chemical Society, Washington DC, pp 57–126

Qu Y, Yin W, Zhang RY, Zhao S, Liu L, Yu J (2020) Isolation and characterization of cellulosic fibers from ramie using organosolv degumming process. Cellulose 27:1225–1237. https://doi.org/10.1007/s10570-019-02835-w

Sandberg D, Haller P, Navi P (2012) Thermo-hydro and thermo-hydro-mechanical wood processing: an opportunity for future environmentally friendly wood products. Wood Mater Sci Eng 8:64–88. https://doi.org/10.1080/17480272.2012.751935

Segmehl JS, Keplinger T, Krasnobaev A, Berg JK, Willa C, Burgert I (2019) Facilitated delignification in CAD deficient transgenic poplar studied by confocal Raman spectroscopy imaging. Spectrochim Acta A Mol Biomol Spectrosc 206(5):177–184. https://doi.org/10.1016/j.saa.2018.07.080

Seki M, Kiryu T, Miki T, Tanaka S, Shigematsu I, Kanayama K (2016) Extrusion of solid wood impregnated with phenol formaldehyde (PF) resin: Effect of resin content and moisture content on extrudability and mechanical properties of extrudate. BioResources 11(3):7697–7709. https://doi.org/10.15376/biores.11.3.7697-7709

Song J, Chen C, Zhu S, Zhu M, Dai J, Ray U, Li Y, Kuang Y, Li Y, Quispe N, Yao Y, Gong A, Leiste UH, Bruck HA, Zhu JY, Vellore A, Li H, Minus ML, Jia Z, Martini A, Li T, Hu L (2018) Processing bulk natural wood into a high-performance structural material. Nature 554:224–228. https://doi.org/10.1038/nature25476

Spear MJ, Eder A, Carus M (2015) 10 - Wood polymer composites. In: Ansell MP (ed) Wood Composites, 1st edn. Woodhead Publishing Elsevier Ltd., Cambridge, pp 195–249

Tarvo V, Lehtimaa T, Kuitunen S, Alopaeus V, Vuorinen T, Aittamaa J (2010) A model for chlorine dioxide delignification of chemical pulp. J Wood Chem Tech 30:230–268. https://doi.org/10.1080/02773810903461476

Xu E, Wang D, Lin L (2020) Chemical structure and mechanical properties of wood cell walls treated with acid and alkali solution. Forests 11(1):87. https://doi.org/10.3390/f11010087

Yamashita O, Yokochi H, Miki T, Kanayama K (2009) The pliability of wood and its application to molding. J Mater Proc Tech 209(12–13):5239–5244. https://doi.org/10.1016/j.jmatprotec.2008.12.011